Available online at www.sciencedirect.com
ScienceDirect
Journal of Sound and Vibration 301 (2007) 927–949
JOURNAL OF SOUND AND VIBRATION
www.elsevier.com/locate/jsvi

Effect of sliding friction on the dynamics of spur gear pair with realistic time-varying stiffness

Song He, Rajendra Gunda, Rajendra Singh*

Acoustics and Dynamics Laboratory, Department of Mechanical Engineering and Center for Automotive Research, The Ohio State University, Columbus, OH 43210, USA

Received 20 December 2005; received in revised form 18 May 2006; accepted 31 October 2006
Available online 28 December 2006

Abstract

The chief objective of this article is to propose a new method of incorporating the sliding friction and realistic time-varying stiffness into an analytical (multi-degree-of-freedom) spur gear model and to evaluate their effects. An accurate finite element/contact mechanics analysis code is employed, in the "static" mode, to compute the mesh stiffness at every time instant under a range of loading conditions. Here, the time-varying stiffness is calculated as an effective function which may also include the effect of profile modifications. The realistic mesh stiffness is then incorporated into the linear time-varying spur gear model with the contributions of sliding friction. Proposed methods are illustrated via two spur gear examples and validated by using the finite element in the "dynamic" mode as experimental results. A key question whether the sliding friction is indeed the source of the off-line-of-action forces and motions is then answered by our analytical model. Finally, the effect of the profile modification on the dynamic transmission error has been analytically examined under the influence of sliding friction. For instance, the linear tip relief introduces an amplification in the off-line-of-action forces and motions due to an out of phase relationship between the normal load and friction forces.

1. Introduction

In a series of recent articles, Vaishya and Singh [1–3] developed a spur gear pair model with periodic tooth stiffness variations and sliding friction based on the assumption that load is equally shared among all the teeth in contact. Using the simplified rectangular pulse shaped variation in mesh stiffness, they solved the single-degree-of-freedom (SDOF) system equations in terms of the dynamic transmission error (DTE) using the Floquet theory and the harmonic balance method [1–3]. While the assumption of equal load sharing yields simplified expressions and analytically tractable solutions, it may not lead to a realistic model. The research reported in this article aims to overcome this deficiency by employing realistic time-varying tooth stiffness functions and the sliding friction over a range of operational conditions. A new linear time-varying (LTV) formulation will be extended to include multi-degree-of-freedom (MDOF) system dynamics for a spur gear pair.

*Corresponding author. Tel.: +1 614 292 9044; fax: +1 614 292 3163.
E-mail address: singh.3@osu.edu (R. Singh).

0022-460X/$ - see front matter © 2006 Elsevier Ltd. All rights reserved.
doi:10.1016/j.jsv.2006.10.043

Vaishya and Singh [1–3] have already provided an extensive review of prior work. In addition, Houser et al. [4] experimentally demonstrated that the friction forces play a pivotal role in determining the load transmitted to the bearings and housing in the off-line-of-action (OLOA) direction; this effect is more pronounced at higher torque and under lower speed conditions. Velex and Cahouet [5] described an iterative procedure to evaluate the effects of sliding friction, tooth shape deviations and time-varying mesh stiffness in spur and helical gears and compared simulated bearing forces with measurements. They reported significant oscillatory bearing forces at lower speeds that are induced by the reversal of friction excitation with alternating tooth sliding direction. In a subsequent study, Velex and Sainsot [6] analytically found that the Coulomb friction should be viewed as a non-negligible excitation source to error-less spur and helical gear pairs, especially for translational vibrations and in the case of high contact ratio gears. However, their work was confined to a study of excitations and the effects of tooth modifications were not considered. Lundvall et al. [7] considered profile modifications and manufacturing errors in a multi-degree-of-freedom spur gear model and examined the effect of sliding friction on the angular dynamic motions. By utilizing a numerical method, they reported that the profile modification has less influence on the dynamic transmission error when frictional effects are included. Nevertheless, two key questions remain unresolved. How to concurrently incorporate the time-varying sliding friction and the realistic mesh stiffness functions into an analytical (MDOF) formulation? How to quantify dynamic interactions between sliding friction and mesh stiffness terms especially when tip relief is provided to the gears? Our article will address these issues.

2. Problem formulation

2.1. Objectives and assumptions

The chief objective of this article is to propose a new method of incorporating the sliding friction and realistic time-varying stiffness into an analytical multi-degree-of-freedom spur gear model and to evaluate their interactions. Key assumptions are: (i) the pinion and gear are modeled as rigid disks; (ii) the shaft-bearings stiffness in the line-of-action (LOA) and off-line-of-action directions are modeled as lumped elements which are connected to a rigid casing; (iii) vibratory angular motions are small in comparison to the mean motion; and (iv) Coulomb friction is assumed with a constant coefficient of friction μ. If assumption (iii) is not made, the system model would have implicit non-linearities. Consequently, the position of the line of contact and relative sliding velocity depend only on the nominal angular motions.

An accurate finite element/contact mechanics (FE/CM) analysis code [8] will be employed in the ''static'' mode to compute the mesh stiffness at every time instant under a range of loading conditions. Here, the time-varying stiffness is calculated as an effective function which may also include the effect of profile modifications. The realistic mesh stiffness is then incorporated into the linear time-varying spur gear model with the contributions of sliding friction. The multi-degree-of-freedom formulation should describe both the line-of-action and off-line-of-action dynamics; a simplified single-degree-of-freedom model will also be derived that describes the vibratory motion in the torsional direction. Proposed methods will be illustrated via two spur gear examples (designated as I and II) whose parameters are listed in Tables 1 and 2. The MDOF model of Example I will be validated by using the finite element/contact mechanics code [8] in the ''dynamic'' mode. Issues related to tip relief will be examined in Example II in the presence of sliding friction. Finally, experimental results for Example II will be used to further validate our method.

2.2. Timing of key meshing events

Analytical formulations for a spur gear pair are derived via Example I (NASA-ART spur gear pair) with the parameters in Table 1. For a generic spur gear pair with non-integer contact ratio σ, $n = \text{ceil}(\sigma)$ meshing tooth pairs need to be considered, where the ''ceil'' function rounds σ value to the nearest integer bigger than σ. Consequently, two meshing tooth pairs need to be modeled for Example I ($\sigma = 1.43$).

First, transitions in key meshing events within a mesh cycle need to be determined from the undeformed gear geometry for the construction of the stiffness function. Fig. 1 is a snapshot for Example I at the beginning

Table 1
Parameters of Example I: NASA-ART spur gear pair (non-unity ratio)

Parameter/property	Pinion	Gear
Number of teeth	25	31
Diametral pitch, in^{-1}	8	8
Pressure angle, deg	25	25
Outside diameter, in	3.372	4.117
Root diameter, in	2.811	3.561
Face width, in	1.250	1.250
Tooth thickness, in	0.196	0.196
Gear mass, $lb\,s^2\,in^{-1}$	6.72E−03	1.04E−02
Polar moment of inertia, $lb\,s^2\,in$	8.48E−03	2.00E−02
Bearing stiffness (LOA and OLOA), $lb\,in^{-1}$	20E6	
Center distance, in	3.5	
Profile contact ratio	1.43	
Elastic modulus, psi	30E6	
Density, $lb\,s^{-2}\,in^{-4}$	7.30E−04	
Poisson's ratio	0.3	

Table 2
Parameters of Example II-A and II-B: NASA spur gear pair (unity ratio). Gear pair with the perfect involute profile is designated as II-A case and the one with tip relief is designated as II-B case

Parameter/property	Pinion/Gear
Number of teeth	28
Diametral pitch, in^{-1}	8
Pressure angle, deg	20
Outside diameter, in	3.738
Root diameter, in	3.139
Face width, in	0.25
Tooth thickness, in	0.191
Roll angle where the tip modification starts (for II-B), deg	24.5
Straight tip modification (for II-B), in	7E−04
Center distance, in	3.5
Profile contact ratio	1.63
Elastic modulus, psi	30E6
Density, $lb\,s^{-2}\,in^{-4}$	7.30E−04
Poisson's ratio	0.3
Range of temperatures, °F	104, 122, 140, 158, 176
Range of input torques, lb in	500, 600, 700, 800, 900

of the mesh cycle ($t = 0$). At that time, pair #1 (defined as the tooth pair rolling along line AC) just comes into mesh at point A and pair #0 (defined as the tooth pair rolling along line CD) is in contact at point C, which is the highest point of single tooth contact (HPSTC). As the gears roll, when pair #1 approaches the lowest point of single tooth contact (LPSTC) of point B at $t = t_B$, pair #0 leaves contact. At $t = t_P$, pair #1 passes through the pitch point P, and the relative sliding velocity of the pinion with respect to the gear is reversed, resulting in a reversal of the friction force. This should provide an impulse excitation to the system. Finally, pair #1 goes through point C at $t = t_c$, completing one mesh cycle (t_c). These key events are defined below, where Ω_p is the nominal pinion speed, r_{bp} is the base radius of the pinion, length L_{AC} is equal to one base pitch λ

$$t_c = \frac{\lambda}{\Omega_p r_{bp}}, \quad \frac{t_b}{t_c} = \frac{L_{AB}}{\lambda}, \quad \frac{t_p}{t_c} = \frac{L_{AP}}{\lambda}. \tag{1a–c}$$

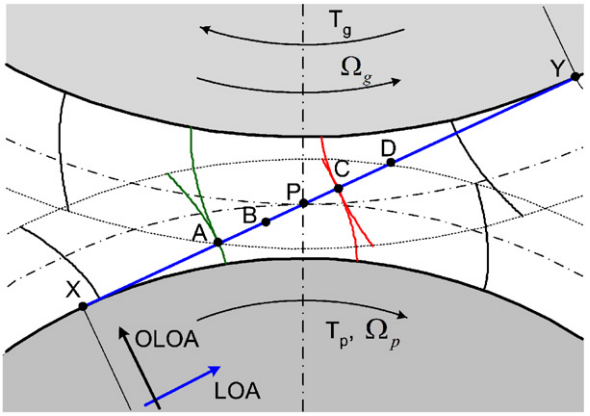

Fig. 1. Snap short of contact pattern (at $t = 0$) in the spur gear pair of Example I.

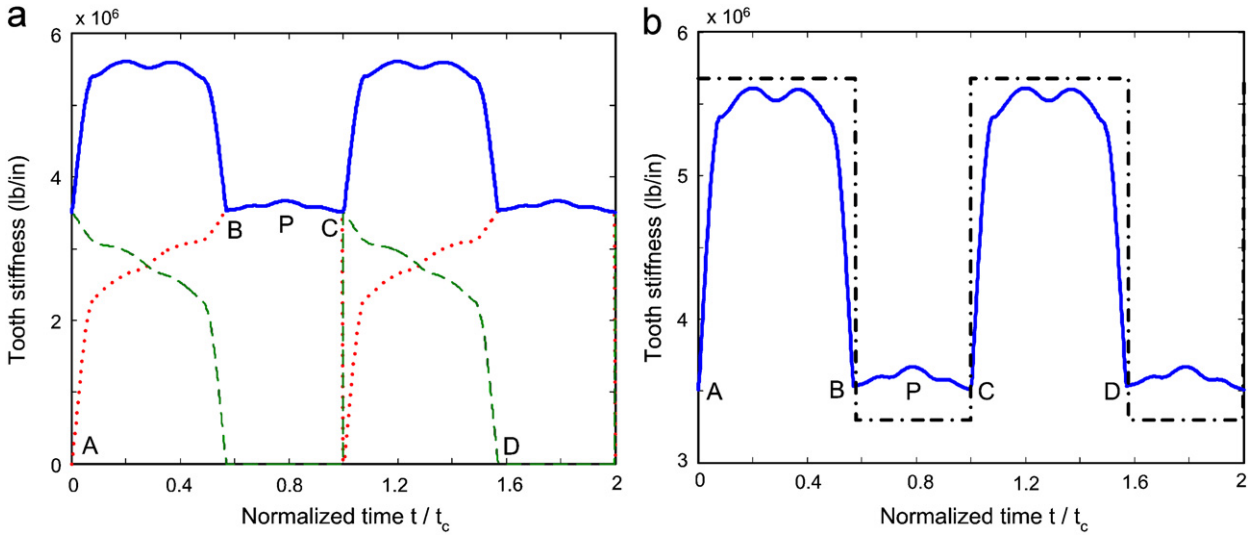

Fig. 2. Tooth mesh stiffness functions of Example I calculated by using the FE/CM code (in the "static" mode). (a) Individual and combined stiffness functions. — total stiffness, ····· stiffness of pair #0, and - - - stiffness of pair #1. (b) The combined stiffness functions. — realistic load sharing and - · - equal load sharing as assumed by Vaishya and Singh [1–3].

2.3. Calculation of realistic time-varying tooth stiffness functions

The realistic time-varying stiffness functions are calculated by using a finite element/contact mechanics code, External2D [8]. An input torque T_p is applied to the pinion rotating at Ω_p, and the mean braking torque T_g on the gear and its angular velocity Ω_g obey the basic gear kinematics. Superposed on the nominal motions are oscillatory components denoted by θ_p and θ_g for the pinion and gear, respectively. The normal contact forces $N_0(t)$, $N_1(t)$ and the pinion deflection $\theta_p(t)$ are then computed by performing a static analysis using the finite element/contact mechanics software [8]. The stiffness function of the ith meshing tooth pair for a generic spur gear pair is given by Eq. (2), where the "floor" function rounds the contact ratio σ down to the nearest (lower) integer value, i.e. floor $(\sigma) = 1$ for Example I

$$k_i(t) = \frac{N_i(t)}{r_{bp}\theta_p(t)}, \quad i = 0, 1, \ldots, n = \text{floor}(\sigma). \tag{2}$$

The stiffness function $k(t)$ for a single tooth pair rolling through the entire meshing process is obtained by following the contact tooth pair for $n = \text{ceil}(\sigma)$ number of mesh cycles where the "ceil" function rounds sigma to the nearest (higher) integer value. Due to the periodicity of the system, the expanded stiffness function $k_i(t)$ of the ith meshing tooth pair is calculated at any time instant t as

$$k_i(t) = k[(n-i)t_c + \text{mod}(t, t_c)], \quad i = 0, 1, \ldots, n = \text{floor}(\sigma). \tag{3}$$

Here, "mod" is the modulus function defined as

$$\text{mod}(x, y) = x - y\,\text{floor}(x/y), \quad \text{if } y \neq 0. \tag{4}$$

For Example I, the calculated $k_0(t)$, $k_1(t)$ functions and their combined stiffness are shown in Fig. 2(a). Note that $k_0(t)$ and $k_1(t)$ are, in fact, different portions of $k(t)$ as described in Eq. (3). In Fig. 2(b) the continuous $k(t)$ of the realistic load sharing model is compared with the rectangular pulse shaped discontinuous $k(t)$ based on the equal load sharing formulation proposed earlier by Vaishya and Singh [1–3].

3. Analytical multi-degree-of-freedom dynamic model

3.1. Shaft and bearing stiffness models

Next, we develop a generic spur gear pair model with 6 degrees-of-freedom including rotational motions (θ_p and θ_g), line-of-action translations (x_p and x_g) and off-line-of-action translations (y_p and y_g). The governing equations are derived in the subsequent sections. First, a simplified shaft model, as shown in Fig. 3, is developed based on the Euler's beam theory [9]. Corresponding to the 6 degrees-of-freedom mentioned above, only the diagonal terms in the shaft stiffness matrix need to be determined and these are given by

$$K_{Sx} = K_{Sy} = 3EI\frac{a+b}{a^3b^3}\left[(a-b)^2 + ab\right], \quad K_{S\theta_z} = 0, \tag{5a,b}$$

where E is the Young's modulus, $I = \pi r_s^4/4$ is the area moment of inertia for the shaft, and a and b are the distances from pinion/gear to the bearings.

The rolling element bearings are modeled by using the bearing stiffness matrix $\mathbf{K}_{Bm}$ formulation (of dimension 6) as proposed by Lim and Singh [10,11]. Assume that each shaft is supported by two identical axially pre-loaded ball bearings with a mean axial displacement, then the mean driving load T_m generates a mean radial force F_{xm} in the line-of-action direction and a moment M_{ym} around the off-line-of-action direction. The time-varying friction force and torque are not included in the mean loads. Corresponding to the 6 degrees-of-freedom considered in our spur gear model, only two significant coefficients, K_{Bxx} and K_{Byy}, are considered for $\mathbf{K}_{Bm}$ [10,11]. The combined bearing-shaft stiffnesses (K_{Bx} and K_{By} in the line-of-action and off-line-of-action directions) are derived by assuming that the bearing and shaft stiffness elements act in series.

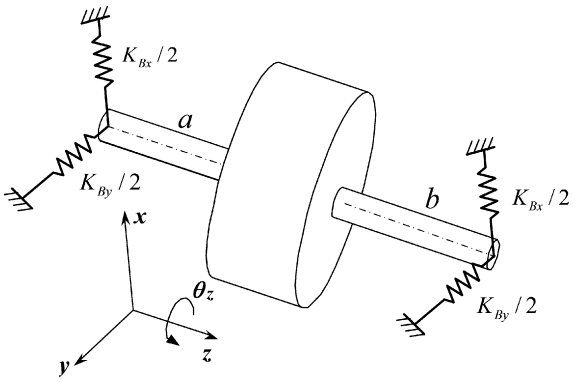

Fig. 3. Schematic of the bearing-shaft model.

3.2. Dynamic mesh and friction forces

Fig. 4 depicts the mean torque and the internal reaction forces acting on the pinion for Example I. For the sake of clarity, forces on the gear are not shown, which are equal in magnitude but opposite in direction to the pinion forces. Based on the Coulomb friction law, the magnitude of friction force (F_f) is proportional to the nominal tooth load (N): $|F_f| = |\mu N|$, where μ is constant. The direction of F_f is determined from the calculation of the nominal relative sliding velocity, which results in the linear-time-varying system formulation. $X_{pi}(t)$ is the moment arm on the pinion for the friction force acting on the ith meshing tooth pair and is given by

$$X_{pi}(t) = L_{XA} + (n-i)\lambda + \mathrm{mod}(\Omega_p r_{bp} t, \lambda), \quad i = 0, 1, \ldots, n = \mathrm{floor}(\sigma). \tag{6}$$

The corresponding moment arm for the friction force on the gear is

$$X_{gi}(t) = L_{YC} + i\lambda - \mathrm{mod}(\Omega_g r_{bg} t, \lambda), \quad i = 0, 1, \ldots, n = \mathrm{floor}(\sigma). \tag{7}$$

Assume, that the mesh (viscous) damping coefficient is time varying and relate it to $k_i(t)$ by a time-invariant damping ratio ζ_m as follows:

$$c_i(t) = 2\zeta_{mi}\sqrt{k_i(t)\cdot J_e}, \quad i = 0, 1, \ldots, n = \mathrm{floor}(\sigma), \tag{8}$$

where $J_e = J_p J_g/(J_p r_{bg}^2 + J_g r_{bp}^2)$.

The normal forces acting on the pinion are

$$\begin{aligned} N_{pi}(t) = N_{gi}(t) = {} & k_i(t)\left[r_{bp}\,\theta_p(t) - r_{bg}\,\theta_g(t) - \varepsilon_p(t) + x_p(t) - x_g(t)\right] \\ & + c_i(t)\left[r_{bp}\,\dot{\theta}_p(t) - r_{bg}\,\dot{\theta}_g(t) - \dot{\varepsilon}_p(t) + \dot{x}_p(t) - \dot{x}_g(t)\right], \quad i = 0, 1, \ldots, n = \mathrm{floor}(\sigma). \end{aligned} \tag{9}$$

Here $\varepsilon_P(t)$ is the profile error component of the static transmission error (STE), and $x_p(t)$ and $x_g(t)$ denote the translational bearing displacements of pinion and gear, respectively. For a generic spur gear pair whose jth meshing pair passes through the pitch point within the mesh cycle, the friction forces in the ith meshing pair

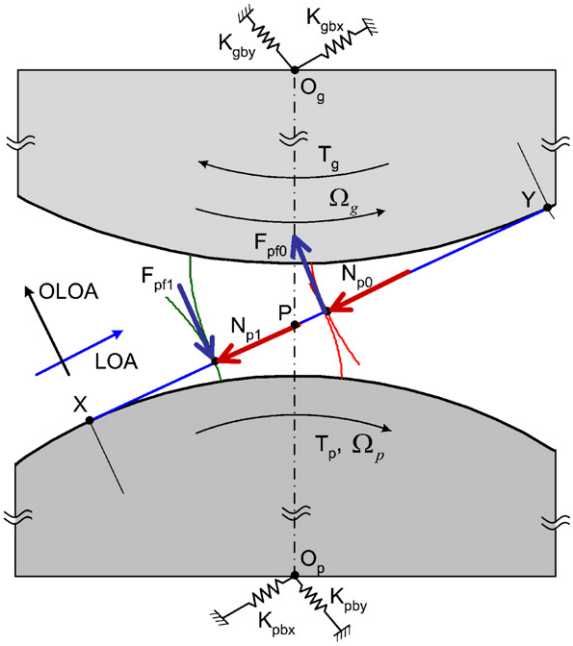

Fig. 4. Normal and friction forces of analytical (MDOF) spur gear system model.

are derived as follows:

$$F_{pfi}(t)=\begin{cases}\mu N_{pi}(t), & i=0,1,\ldots,j-1,\\ \mu N_{pi}(t)\mathrm{sgn}\left[\mathrm{mod}(\Omega_p r_{bp}t,\lambda)+(n-i)\lambda-L_{AP}\right], & i=j,\\ -\mu N_{pi}(t), & i=j,j+1,\ldots,n=\mathrm{floor}(\sigma),\end{cases} \tag{10a}$$

$$F_{gfi}(t)=\begin{cases}\mu N_{gi}(t), & i=0,1,\ldots,j-1,\\ \mu N_{gi}(t)\mathrm{sgn}\left[\mathrm{mod}(\Omega_g r_{bg}t,\lambda)+(n-i)\lambda-L_{AP}\right], & i=j,\\ -\mu N_{gi}(t), & i=j,j+1,\ldots,n=\mathrm{floor}(\sigma).\end{cases} \tag{10b}$$

Consequently, the friction forces for Example I of Fig. 4 are given as

$$F_{pf0}(t)=\mu N_{p0}(t),\quad F_{pf1}(t)=\mu N_{p1}(t)\mathrm{sgn}\left[\mathrm{mod}(\Omega_p r_{bp}t,\lambda)-L_{AP}\right], \tag{10c,d}$$

$$F_{gf0}(t)=\mu N_{g0}(t),\quad F_{gf1}(t)=\mu N_{g1}(t)\mathrm{sgn}\left[\mathrm{mod}(\Omega_g r_{bg}t,\lambda)-L_{AP}\right]. \tag{10e,f}$$

3.3. Multi-degree-of-freedom model

The governing equations for the torsional DOFs are

$$J_p\ddot{\theta}_p(t)=T_p+\sum_{i=0}^{n=\mathrm{floor}(\sigma)}X_{pi}(t)\,F_{pfi}(t)-\sum_{i=0}^{n=\mathrm{floor}(\sigma)}r_{bp}\,N_{pi}(t), \tag{11}$$

$$J_g\ddot{\theta}_g(t)=-T_g+\sum_{i=0}^{n=\mathrm{floor}(\sigma)}X_{gi}(t)\,F_{gfi}(t)+\sum_{i=0}^{n=\mathrm{floor}(\sigma)}r_{bg}\,N_{gi}(t). \tag{12}$$

The governing equations of the translational DOFs in the LOA direction are

$$m_p\ddot{x}_p(t)+2\zeta_{pBx}\sqrt{K_{pBx}\,m_p}\,\dot{x}_p(t)+K_{pBx}x_p(t)+\sum_{i=0}^{n=\mathrm{floor}(\sigma)}N_{pi}(t)=0, \tag{13}$$

$$m_g\ddot{x}_g(t)+2\zeta_{gBx}\sqrt{K_{gBx}\,m_g}\,\dot{x}_g(t)+K_{gBx}x_g(t)+\sum_{i=0}^{n=\mathrm{floor}(\sigma)}N_{gi}(t)=0. \tag{14}$$

Here, K_{pBx} and K_{gBx} are the effective shaft-bearing stiffnesses in the line-of-action direction as discussed in Section 3.1, and ζ_{pBx} and ζ_{gBx} are their damping ratios. Similarly, the governing equations of the translational DOFs in the off-line-of-action direction are

$$m_p\ddot{y}_p(t)+2\zeta_{pBy}\sqrt{K_{pBy}\,m_p}\,\dot{y}_p(t)+K_{pBy}y_p(t)-\sum_{i=0}^{n=\mathrm{floor}(\sigma)}F_{pfi}(t)=0, \tag{15}$$

$$m_g\ddot{y}_g(t)+2\zeta_{gBy}\sqrt{K_{gBy}\,m_g}\,\dot{y}_g(t)+K_{gBy}y_g(t)-\sum_{i=0}^{n=\mathrm{floor}(\sigma)}F_{gfi}(t)=0. \tag{16}$$

The composite DTE, which is the relative dynamic displacement of pinion and gear along the LOA direction, is defined as

$$\delta(t)=r_{bp}\theta_p(t)-r_{bg}\theta_g(t)+x_p(t)-x_g(t). \tag{17}$$

Finally, the dynamic bearing forces are given by

$$F_{pBx}(t)=-K_{pBx}\,x_p(t)-2\zeta_{pBx}\sqrt{K_{pBx}m_p}\,\dot{x}_p(t), \tag{18a}$$

$$F_{pBy}(t)=-K_{pBy}\,y_p(t)-2\zeta_{pBb}\sqrt{K_{pBy}m_p}\,\dot{y}_p(t), \tag{18b}$$

$$F_{gBx}(t) = -K_{gBx}\,x_g(t) - 2\zeta_{gBb}\sqrt{K_{gBx}m_g}\,\dot{x}_g(t), \tag{18c}$$

$$F_{gBy}(t) = -K_{gBy}\,y_g(t) - 2\zeta_{gBb}\sqrt{K_{gBy}m_g}\,\dot{y}_g(t). \tag{18d}$$

4. Analytical single-degree-of-freedom torsional model

When only the torsional degrees-of-freedom of the spur gear pair are of interest, a simplified but equivalent single-degree-of-freedom model can be derived by assuming that the shaft-bearing's stiffness is much higher than the mesh stiffness. After expressing $\theta_p(t)$ and $\theta_g(t)$ in terms of the dynamic transmission error, $\delta(t) = r_{bp}\theta_p(t) - r_{bg}\theta_g(t)$, the governing single-degree-of-freedom model is obtained for a generic spur gear pair whose jth meshing pair passes through the pitch point within the mesh cycle

$$\begin{aligned}
&J_e\ddot{\delta}(t) + \sum_{i=0}^{n=\mathrm{floor}(\sigma)}\left[c_i(t)\dot{\delta}(t) + k_i(t)\delta(t)\right] \\
&\quad + \mu\sum_{i=0}^{n=\mathrm{floor}(\sigma)}\left\{\mathrm{sgn}\left[\mathrm{mod}(\Omega_p r_{bp}t,\lambda) + (n-j)\lambda - L_{AP}\right]\left[c_i(t)\dot{\delta}(t) + k_i(t)\delta(t)\right]\right. \\
&\quad \left.\times\left[\frac{X_{pj}(t)J_g r_{bp} + X_{gj}(t)J_p r_{bg}}{J_p r_{bg}^2 + J_g r_{bp}^2}\right]\right\} \\
&= \frac{T_e}{J_p r_{bg}^2 + J_g r_{bp}^2} + \sum_{i=0}^{n=\mathrm{floor}(\sigma)}\left[c_i(t)\dot{\varepsilon}_p(t) + k_i(t)\varepsilon_p(t)\right] \\
&\quad + \mu\sum_{i=0}^{n=\mathrm{floor}(\sigma)}\left\{\mathrm{sgn}\left[\mathrm{mod}(\Omega_p r_{bp}t,\lambda) + (n-j)\lambda - L_{AP}\right]\left[c_i(t)\dot{\varepsilon}_p(t) + k_i(t)\varepsilon_p(t)\right]\right. \\
&\quad \left.\times\left[\frac{X_{pj}(t)J_g r_{bp} + X_{gj}(t)J_p r_{bg}}{J_p r_{bg}^2 + J_g r_{bp}^2}\right]\right\}.
\end{aligned} \tag{19}$$

Here the effective polar moment of inertia J_e is consistent with that defined in Eq. (8) and the effective torque is $T_e = T_p J_g r_{bp} + T_g J_p r_{bg}$. The dynamic response $\delta(t)$ is controlled by three excitations: (i) time-varying T_e, (ii) $\varepsilon_p(t)$ and its derivative $\dot{\varepsilon}_p(t)$ and (iii) sliding friction. For Example I, the governing equation (19) could be simplified as

$$\begin{aligned}
&J_e\ddot{\delta}(t) + [c_1(t) + c_0(t)]\dot{\delta}(t) + [k_1(t) + k_0(t)]\delta(t) \\
&\quad + \mu\left[c_1(t)\dot{\delta}(t) + k_1(t)\delta(t)\right]\left[\frac{X_{p1}(t)J_g r_{bp} + X_{g1}(t)J_p r_{bg}}{J_p r_{bg}^2 + J_g r_{bp}^2}\right]\mathrm{sgn}\left[\mathrm{mod}(\Omega_p r_{bp}t,\lambda) - L_{AP}\right] \\
&\quad + \mu\left[c_0(t)\dot{\delta}(t) + k_0(t)\delta(t)\right]\frac{\left(X_{p0}(t)J_g r_{bp} + X_{g0}(t)J_p r_{bg}\right)}{J_p r_{bg}^2 + J_g r_{bp}^2} \\
&= \frac{T_e}{J_p r_{bg}^2 + J_g r_{bp}^2} + [c_1(t) + c_0(t)]\dot{\varepsilon}_p(t) + [k_1(t) + k_0(t)]\varepsilon_p(t) \\
&\quad + \mu\left[c_1(t)\dot{\varepsilon}_p(t) + k_1(t)\varepsilon_p(t)\right]\left[\frac{X_{p1}(t)J_g r_{bp} + X_{g1}(t)J_p r_{bg}}{J_p r_{bg}^2 + J_g r_{bp}^2}\right]\mathrm{sgn}\left[\mathrm{mod}(\Omega_p r_{bp}t,\lambda) - L_{AP}\right] \\
&\quad + \mu\left[c_0(t)\dot{\varepsilon}_p(t) + k_0(t)\varepsilon_p(t)\right]\frac{\left(X_{p0}(t)J_g r_{bp} + X_{g0}(t)J_p r_{bg}\right)}{J_p r_{bg}^2 + J_g r_{bp}^2}.
\end{aligned} \tag{20}$$

5. Effect of sliding friction in Example I

5.1. Validation of Example I model using the finite element/contact mechanics code

The governing equations of either the single- or multi-degree-of-freedom system models are numerically integrated by using a 4th–5th order Runge–Kutta algorithm with a fixed time step. The $\varepsilon_p(t)$ and $\dot{\varepsilon}_p(t)$ components are neglected, i.e. no manufacturing errors other than specified profile modifications are considered. Concurrently, the dynamic responses are independently calculated by running the finite element/contact mechanics code [8] and using the Newmark method. Predicted and computed dynamic transmission error, and line-of-action and off-line-of-action forces are in good agreement, as shown in Figs. 5–7. Note that time domain results include both transient and steady state responses but the frequency domain results only include the steady state responses. From Fig. 5 it can be seen that the sliding friction introduces additional dynamic transmission error oscillations when the contact teeth pass through the pitch point. Fig. 6 illustrates that the sliding friction enhances the dynamic bearing forces in the line-of-action direction, especially at the second mesh harmonic. This is because that the moments associated with $F_{pfi}(t)$ and $F_{gfi}(t)$ are coupled with the moments of $N_{pi}(t)$ and $N_{gi}(t)$. Further, the normal loads mainly excite the vibration in the line-of-action direction, as illustrated by Eqs. (9), (11) and (13). The scales of the bearing forces shown in Figs. 7(a–b) for the $\mu = 0$ case are the same as those shown in Figs. 7(c–d) for ease of comparison. The bearing forces predicted by

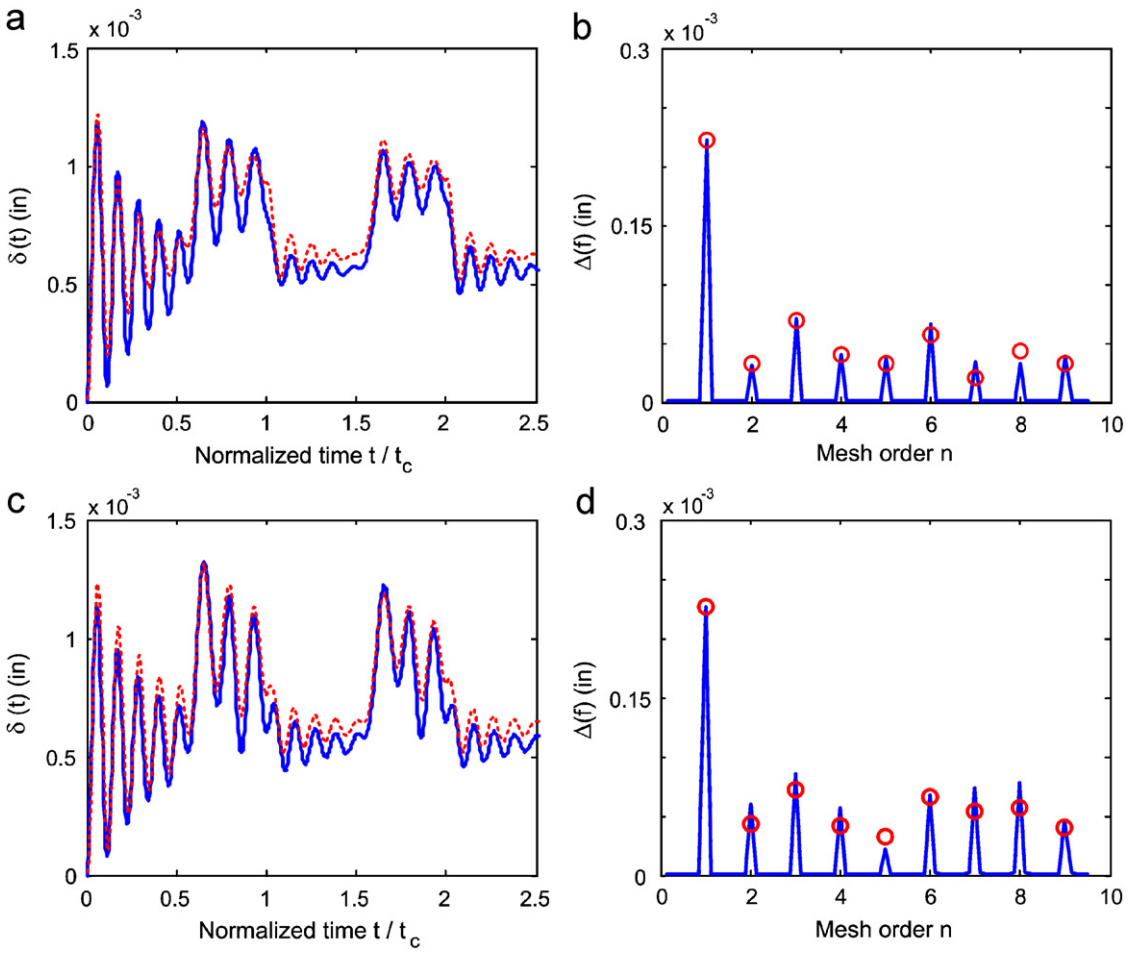

Fig. 5. Validation of the analytical (MDOF) model by using the FE/CM code (in the "dynamic" mode). Here, results for Example I are given in terms of $\delta(t)$ and its spectral contents $\Delta(f)$ with $t_c = 2.4$ ms and $f_m = 416.7$ Hz. Sub-figures (a–b) are for $\mu = 0$ and (c–d) are for $\mu = 0.2$. — Analytical (MDOF) model, ····· FE/CM code (in t domain), and ○ FE/CM code (in f domain).

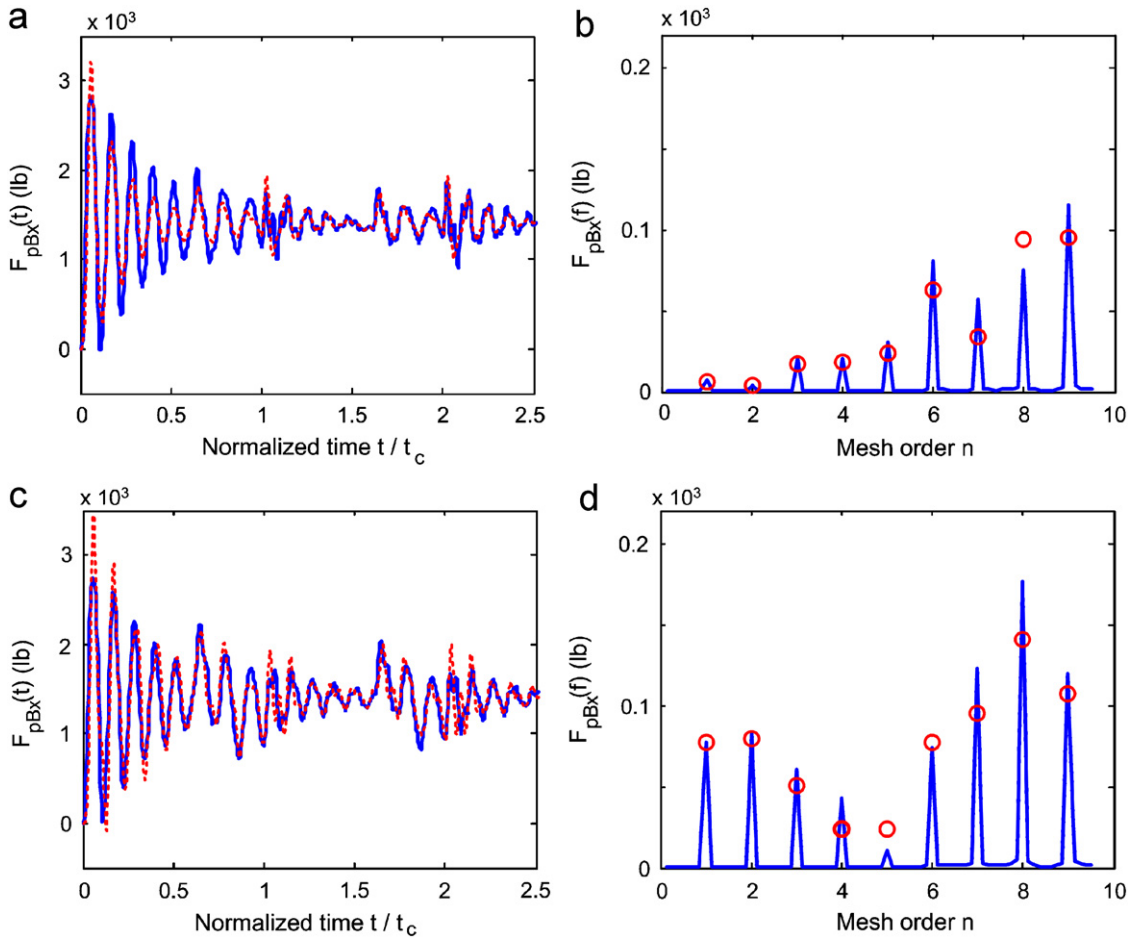

Fig. 6. Validation of the analytical (MDOF) model by using the FE/CM code (in the "dynamic" mode). Here, results for Example I are given in terms of $F_{pBx}(t)$ and its spectral contents $F_{pBx}(f)$ with $t_c = 2.4$ ms and $f_m = 416.7$ Hz. Sub-figures (a–b) are for $\mu = 0$ and (c–d) are for $\mu = 0.2$. — Analytical (MDOF) model, ····· FE/CM code (in t domain) and ○ FE/CM code (in f domain).

the multi-degree-of-freedom model for $\mu = 0$ case approach zero (within the numerical error range). This is consistent with the mathematical description of Eqs. (15) and (16). Larger deviations at this point are observed in Figs. 7(a–b) for the finite element/contact mechanics analysis. As shown in Fig. 7 the off-line-of-action dynamics are more significantly influenced by the sliding friction than the line-of-action dynamics, which are shown in Fig. 6. In order to accurately predict the higher mesh harmonics, refined time steps (e.g., more than 100 increments per mesh cycle) are needed. Consequently, the finite element/contact mechanics analysis tends to generate an extremely large data file that demands significant computing time and post-processing work. Meanwhile, the lumped model allows for much finer time resolution while being computationally more efficient (by at least two orders of magnitude when compared with the finite element/contact mechanics calculations). Hence, the lumped model could be effectively used to conduct parametric design studies.

5.2. *Effect of sliding friction*

Fig. 8 shows the calculated dynamic transmission error without an friction, which is almost identical to the static transmission error at a very low speed ($\Omega_p = 2.4$ rpm). However, the sliding friction changes the shape of the dynamic transmission error curve. During the time interval $t \in [0, t_P]$, the friction torque on the pinion opposes the normal load torque as shown in Fig. 4, resulting in a higher value of the normal load that is needed to maintain the static equilibrium. Also, friction increases the peak-to-peak value of the dynamic

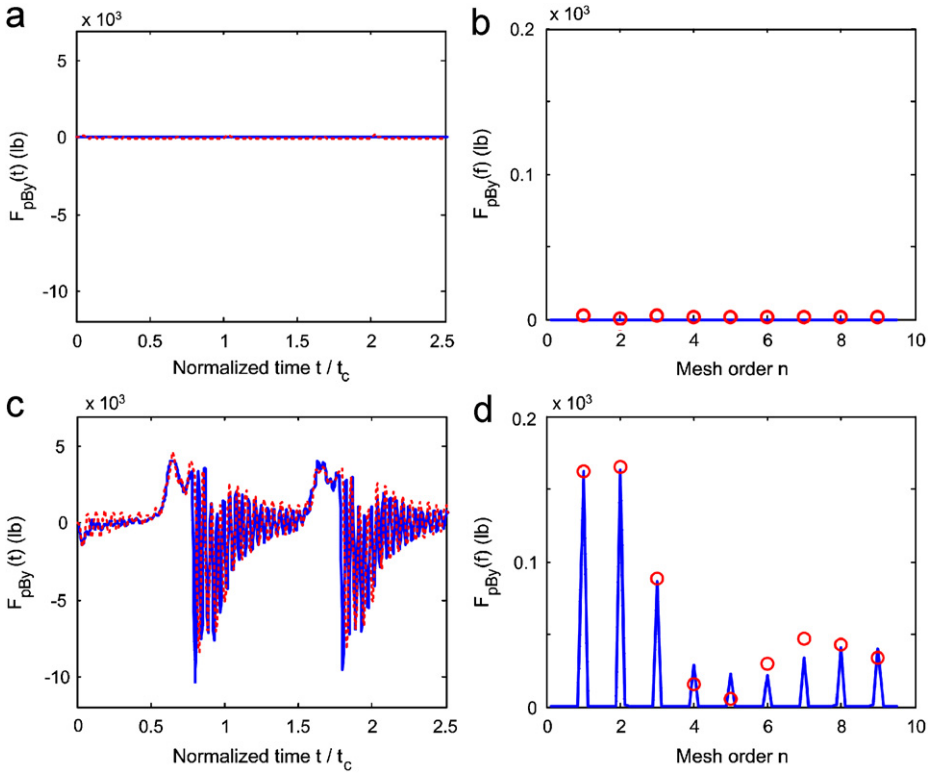

Fig. 7. Validation of the analytical (MDOF) model by using the FE/CM code (in the "dynamic" mode). Here, results for Example I are given in terms of $F_{pBy}(t)$ and its spectral contents $F_{pBy}(f)$ with $t_c = 2.4$ ms and $f_m = 416.7$ Hz. Sub-figures (a–b) are for $\mu = 0$ and (c–d) are for $\mu = 0.2$. — Analytical (MDOF) model, ····· FE/CM code (in t domain) and ○ FE/CM code (in f domain).

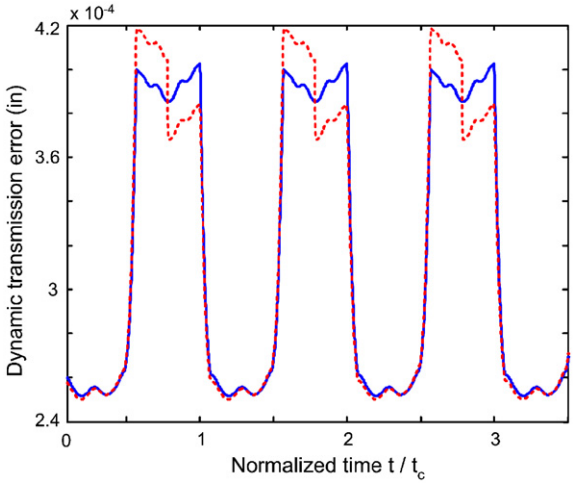

Fig. 8. Effect of μ on $\delta(t)$ based on the linear time-varying SDOF model for Example I at $T_p = 2000$ lb-in. Here, $t_c = 1$ s. — $\mu = 0$ and ····· $\mu = 0.1$.

transmission error compared with that of the static transmission error. For the remainder of the mesh cycle $t \in [t_P, t_c]$, friction torque acts in the same direction as the normal load torque. Thus a small value of the normal load is sufficient to maintain the static equilibrium. Detailed parametric studies show that the amplitude of second mesh harmonic increases with the effect of sliding friction.

5.3. Multi-degree-of-freedom system resonances

For Example I, the nominal bearing stiffness $K_{pBx} = K_{pBy} = K_{gBx} = K_{gBy} = 20 \times 10^6$ lb/in are much higher than the averaged mesh stiffness k_m. The couplings between the rotational and translational degrees-of-freedom in the line-of-action direction are examined by using a simplified 3 degree-of-freedom model as suggested by Kahraman and Singh [12]. Note that the dynamic transmission error is defined as $\delta = r_{bp}\theta_{xp} - r_{bg}\theta_{xg}$, and the undamped equations of motion are

$$\begin{bmatrix} m_e & 0 & 0 \\ 0 & m_p & 0 \\ 0 & 0 & m_g \end{bmatrix} \begin{Bmatrix} \ddot{\delta} \\ \ddot{x}_p \\ \ddot{x}_g \end{Bmatrix} + \begin{bmatrix} k_m & k_m & -k_m \\ k_m & (k_m + K_{pBx}) & -k_m \\ -k_m & -k_m & (k_m + K_{gBx}) \end{bmatrix} \begin{Bmatrix} \delta \\ x_p \\ x_g \end{Bmatrix} = \begin{Bmatrix} 0 \\ 0 \\ 0 \end{Bmatrix}. \tag{21}$$

The effective mass is defined as $m_e = J_p J_g/(r_g^2 J_p + r_p^2 J_g)$. The eigensolutions of Eq. (21) yield three natural frequencies: Two coupled transverse-torsional modes (f_1 and f_3) and one purely transverse mode (f_2); numerical values are: $f_1 = 5130$ Hz, $f_2 = 8473$ Hz and $f_3 = 11{,}780$ Hz. Predictions from Eq. (21) match well with the numerical simulations using the formulations of Section 3 (though these results are not shown here). A comparative study verifies that one natural frequency of the multi-degree-of-freedom model shifts away from that of the single-degree-of-freedom model (6716 Hz) due to the torsional–translational coupling effects. In the off-line-of-action direction, simulation shows that only one resonance is present at $f_{pBy} = (1/2\pi)\sqrt{K_{pBy}/m_p} = 9748$ Hz, which is dictated by the bearing-shaft stiffness.

6. Effect of sliding friction in Example II

Next, the proposed model is applied to Example II with the parameters of Table 2. The chief goal is to examine the effects of tip relief and sliding friction. Further, analogous experiments were conducted on the NASA Glenn Research Center Gear Noise Rig [13]. Comparisons with measurements will be given in Section 7.

6.1. Empirical coefficient of friction

The coefficient of friction varies as the gears travel through mesh, due to constantly changing lubrication conditions between the contact teeth. An empirical equation for the prediction of the dynamic friction variable, μ, under mixed lubrication has been suggested by Benedict and Kelley [14] based on a curve-fit of friction measurements on a roller test machine. Rebbechi et al. [15] verified this formulation by measuring the dynamic friction forces on the teeth of a spur gear pair. Their measurements seem to be in good agreement with the Benedict and Kelley equation except at the meshing positions close to the pitch point. This empirical equation, then modified to account for the average gear tooth surface roughness (R_{avg}), is

$$\mu(\gamma) = 0.0127\, C_{R_{\text{avg}}} \log_{10}\left(\frac{3.17 \times 10^8 X_\Gamma(\gamma) W_n}{\upsilon_o V_s(\gamma) V_e^2(\gamma)}\right), \quad C_{R_{\text{avg}}} = \frac{44.5}{44.5 - R_{\text{avg}}}, \tag{22a,b}$$

where $C_{R_{\text{avg}}}$ is the surface roughness constant, W_n is the normal load per unit length of face width, and υ_0 is the dynamic viscosity of the lubricant. Here $V_s(\gamma)$ is the sliding velocity, defined as the difference in the tangential velocities of the pinion and gear, and $V_e(\gamma)$ is the entraining velocity, defined as the addition of the tangential velocities, for roll angle γ along the line-of-action. Further, R_{avg} in our case was measured with a profilometer by using a standard method described in Ref. [13]. Lastly, $X_\Gamma(\gamma)$ is the load sharing factor as a function of roll angle, and it was assumed based on the ideal profile of smooth meshing gears. In Fig. 9 μ is shown as a function of roll angle calculated by using Eq. (22). Since μ was assumed to be a constant earlier, an averaged value is found by taking an average over the roll angles. The μ values that were computed at each mean torque and oil temperature for Example II (with $R_{\text{avg}} = 0.132\,\mu$m) are given in Table 3.

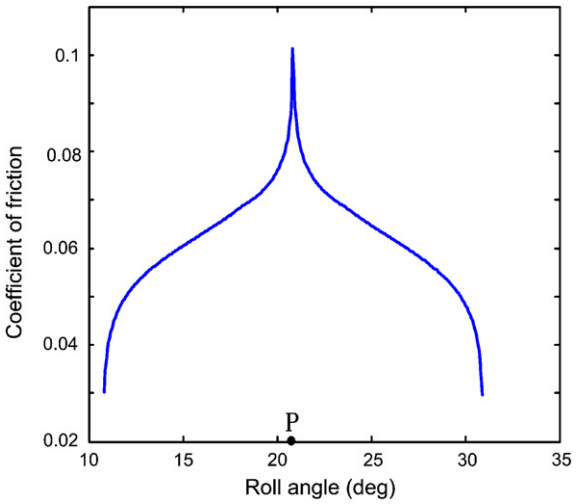

Fig. 9. The coefficient of friction μ as a function of the roll angle for Example II, as predicted by using Benedict & Kelley's empirical equation [14]. Here, oil temperature is 104 °F and $T = 500$ lb-in. P: Pitch point at 20.85°.

Table 3
Averaged coefficient of friction μ predicted over a range of operating conditions for Example II by using Benedict and Kelly's empirical equation [14]

Temperature (°F)	Torque (lb-in)				
	500	600	700	800	900
104	0.032	0.033	0.034	0.035	0.036
122	0.034	0.036	0.037	0.037	0.038
140	0.036	0.037	0.038	0.039	0.040
158	0.038	0.040	0.041	0.041	0.042
176	0.040	0.041	0.042	0.043	0.044

6.2. *Effect of tip relief on STE and k(t)*

The static transmission error is calculated as a function of mean torque for both the perfect involute gear pair (designated as II-A) and then one with tip relief (designated as II-B) by using the Finite element/contact mechanics code. The amplitudes of the static transmission error spectra at mesh harmonics for both cases are shown in Fig. 10. (In this and following figures, predictions are shown as continuous lines for the sake of clarity though they are calculated only at discrete torque points). The first two mesh harmonics are most significantly affected by the tip relief and they are minimal at the "optimal" mean torque around 500 lb-in. For both II-A and II-B cases, typical $k(t)$ functions of a single meshing tooth over two complete mesh cycles are calculated by using Eq. (2) for various mean torques, as shown in Fig. 11. Note that $k(t)$ is defined as the effective stiffness since it incorporates the effects of profile modification such as linear tip relief (II-B). Observe that although the maximum stiffness remains the same, application of the tip relief significantly changes the stiffness profile. For the perfect involute profile (II-A), steep slopes are observed in the vicinities near the single or two teeth contact regimes, and a smooth transition is observed in between these steep regimes. Also, $k(t)$ is found to be insensitive to a variation in the mean torque. However, with tip relief, an almost constant slope is found throughout the transition profile between the single and two teeth contact regimes. Moreover, a smaller profile contact ratio (around 1.1 at 100 lb-in) is observed for the tip relief case when compared with around 1.6 (at all loads) for the perfect involute pair. The realistic $k(t)$ function is then incorporated into the lumped multi-degree-of-freedom dynamic model.

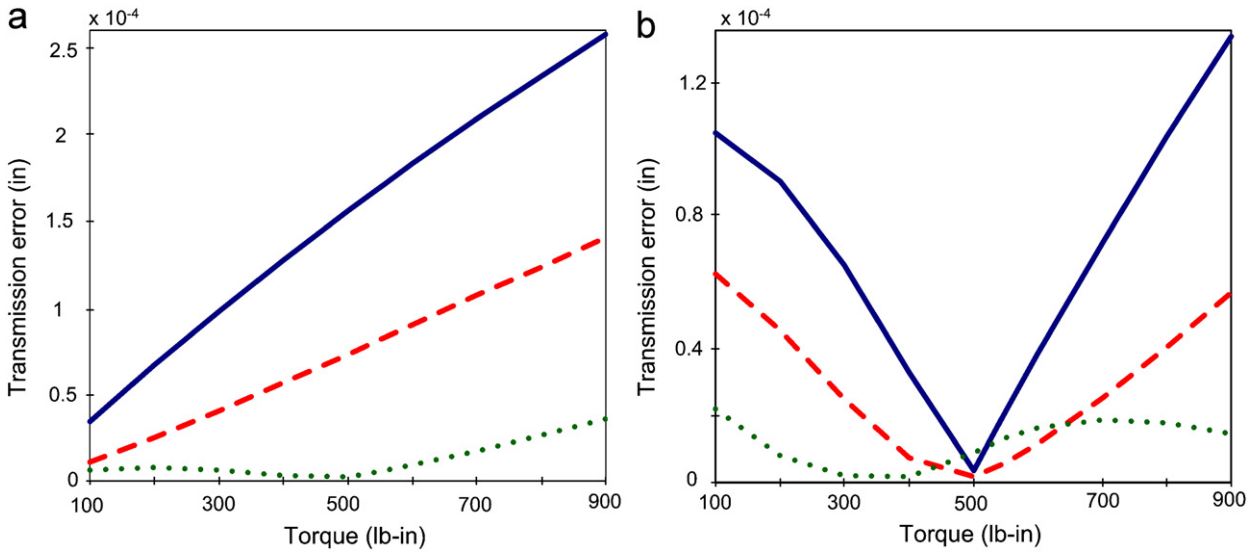

Fig. 10. Mesh harmonics of the static transmission error (STE) calculated by using the FE/CM code (in the "static" mode) for Example II: (a) gear pair with perfect involute profile (II-A) and (b) gear pair with tip relief (II-B). — $n = 1$, -- $n = 2$, and ····· $n = 3$.

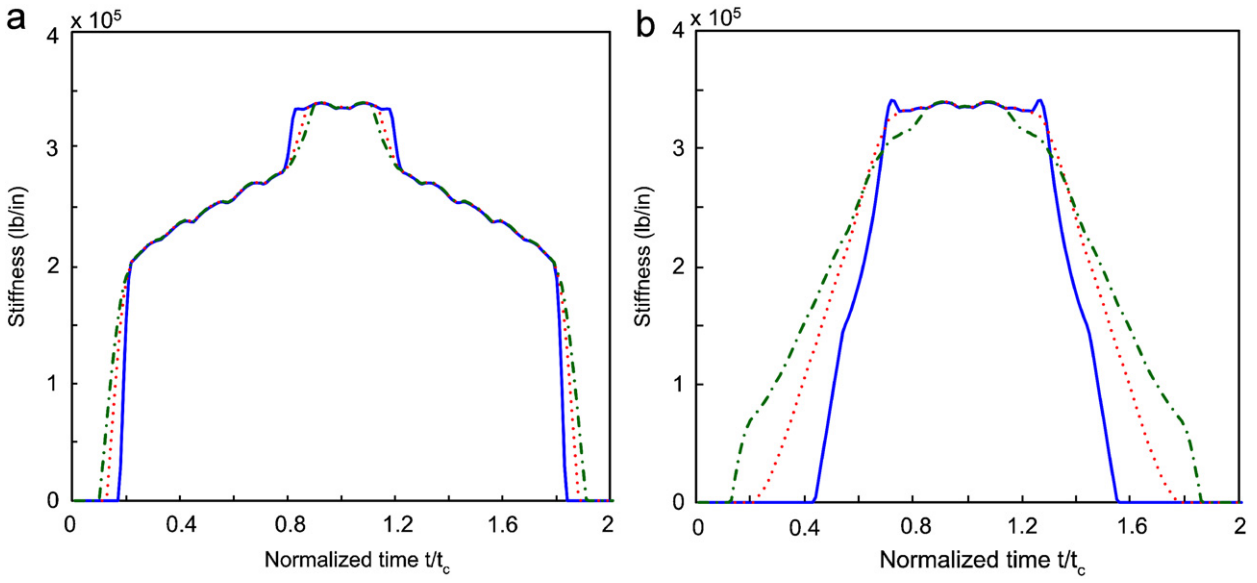

Fig. 11. Tooth stiffness functions of a single mesh tooth pair for Example II: (a) gear pair with perfect involute profile (II-A); (b) gear pair with tip relief (II-B). — 100 lb-in, ····· 500 lb-in, and - - - 900 lb-in.

In Fig. 12 the combined $k(t)$ is shown with contributions of both meshing tooth pairs over two mesh cycles for Example II. Observe that the profile of case II-A is insensitive to a variation in the mean torque, but the profile of case II-B has a minimum around 500 lbf-in. Frequency domain analysis reveals that the first two mesh harmonics are most significantly affected by the linear tip modification. Overall, it is evident that significant changes take place in the static transmission error, tooth load distribution and mesh stiffness function because of the profile modification (tip relief), which may be explained by an avoidance of the corner contact at an "optimized" mean torque.

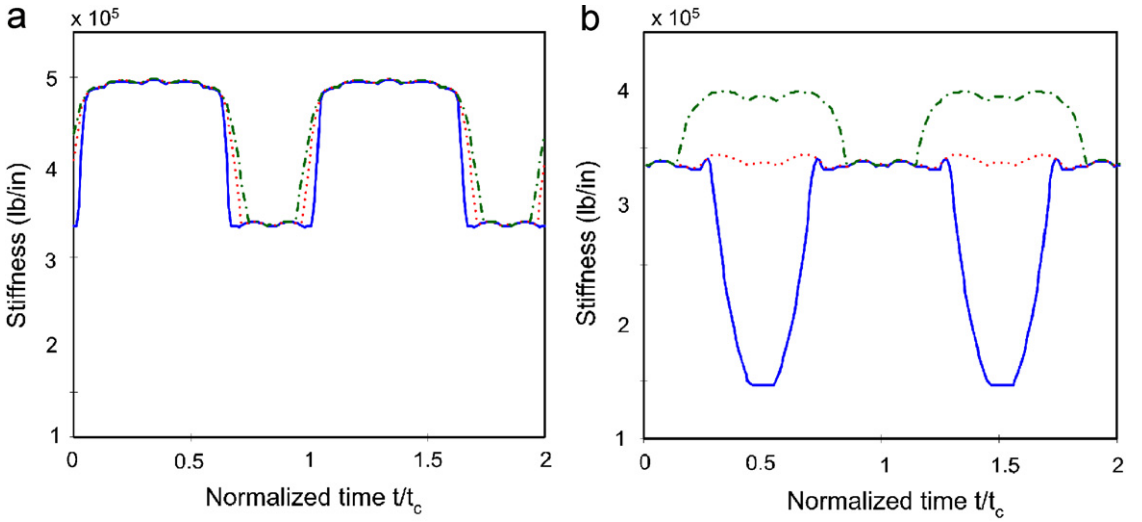

Fig. 12. Combined tooth stiffness functions for Example II: (a) gear pair with perfect involute profile (II-A); (b) gear pair with tip relief (II-B). — 100 lb-in, - - - 500 lb-in, and - - 900 lb-in.

6.3. Phase relationship between normal load and friction force excitations

Using the 6 degree-of-freedom spur gear model with parameters consistent with the experimental conditions, dynamic studies are conducted for Example II. First, a mean torque of 500 lbf-in is used corresponding to the "optimal" case with minimal static transmission error. Eqs. (13)–(16) show that the normal loads $\sum N_i$ and friction forces $\sum F_{fi}$ excite the line-of-action and off-line-of-action dynamics, respectively. The force profile of a single tooth pair undergoing the entire meshing process is obtained for tooth pairs #0 and #1 for two continuous meshing cycles as shown in Figs. 13(a–b) and (c–d) for cases II-A and II-B, respectively. Observe that the peak-to-peak magnitude of combined pinion normal load $\sum N_{pi}$ is minimized for the tip relief gear due to the reduced static transmission error at 500 lb-in. However, the combined pinion friction force $\sum F_{fpi}$ with tip relief has a higher peak-to-peak magnitude when compared with the perfect involute gear. This implies that the tip relief amplifies $\sum F_{fi}$ in the off-line-of-action direction while minimizing $\sum N_i$ in the line-of-action direction. Such contradictory effects are examined next by using the phase relationship between N_{pi} and F_{fpi}.

At points A, B, C and D, corner contacts are observed for N_{pi} of the perfect involute gear, corresponding to the time instants when meshing tooth pairs come into or out of contact. These introduce discontinuous points in the slope of the $\sum N_{pi}$ profile. Note that N_{p1} and N_{p2} between A and B (or C and D) are in phase with each other, which should amplify the peak-to-peak variation of $\sum N_{pi}$. For the F_{fpi} profile of Fig. 13(a), an abrupt change in the direction is observed at the pitch point P in addition to the corner contacts. Unlike N_{pi}, the profiles of F_{fp1} and F_{fp2} of Fig. 13(c) between A and B (or C and D) are out of phase with each other. This should minimize the peak-to-peak variation of $\sum F_{fpi}$. When tip relief is applied in Fig. 13(b), corner contacts of N_{pi} are reduced and smoother transitions are observed at points A, B, C and D. Unlike the perfect involute gear, N_{p1} and N_{p2} are now out of phase with each other between A and B (or C and D), which reduces the peak-to-peak variation of $\sum N_{pi}$. However, the profiles of F_{fp1} and F_{fp2} of Fig. 13(d) are in phase with each other in the same region, which amplifies the variation of $\sum F_{fpi}$. The out of phase relationship between N_{pi} and F_{fpi} explains why the tip relief (designed to minimize the static transmission error) tends to increase the friction force excitations. This relationship is mathematically embedded in Eq. (10) and graphically illustrated in Fig. 4, whereN_{p1} and N_{p2} are in phase while F_{fp1} and F_{fp2} are out of phase. Consequently, a compromise would be needed to simultaneously address the dynamic responses in both the line-of-action and off-line-of-action directions.

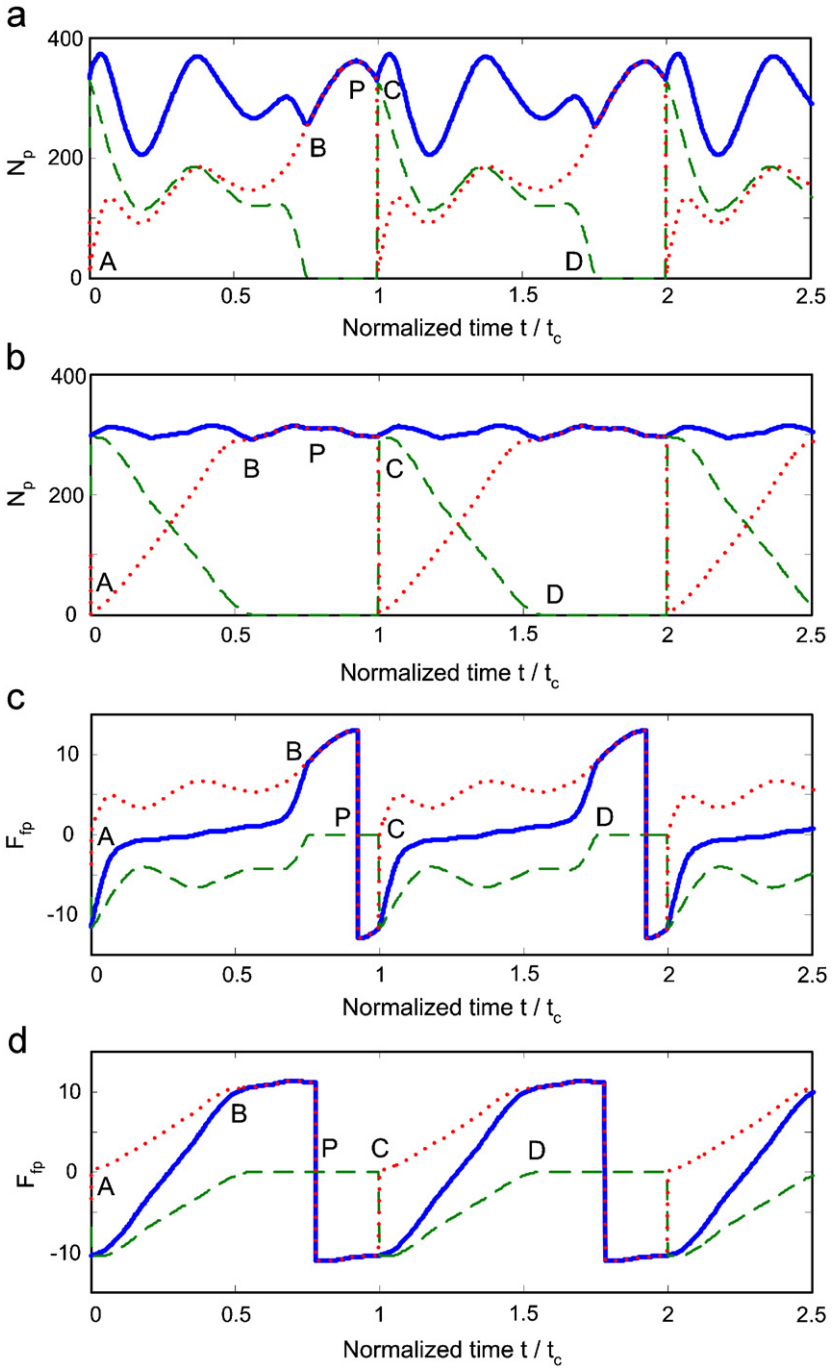

Fig. 13. Dynamic loads predicted for Example II at 500 lb-in, 4875 RPM and 140 °F with $t_c = 0.44$ ms: (a) Normal loads of gear pair with perfect involute profile (II-A), (b) normal loads of gear par with tip relief (II-B), and (c) friction forces of gear pair with perfect involute profile (II-A); (d) friction forces of gear pair with tip relief (II-B). — combined, ····· tooth pair #0 and - - tooth pair #1.

6.4. Prediction of the dynamic responses

Dynamic responses including $x_p(t)$, $y_p(t)$, $F_{pbx}(t)$, $F_{pby}(t)$ and the dynamic transmission error $\delta(t)$ are predicted by numerically integrating the governing equations. Predictions from both perfect and tip relief

gears are compared to examine the effect of profile modification in the presence of sliding friction. From Fig. 14 it can be seen that the normalized $x_p(t)$ at 500 lb-in is much smaller (over 90% reduction) when the tip relief is applied. This is because that the STE is the most dominant excitation in the line-of-action

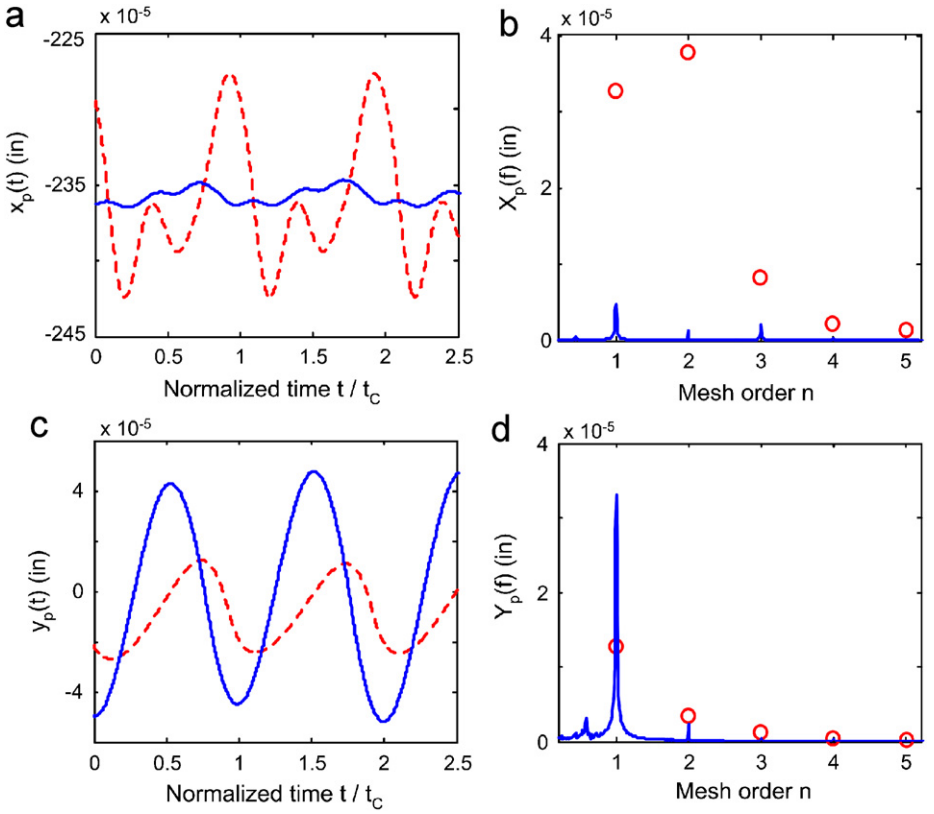

Fig. 14. Dynamic shaft displacements predicted for Example II at 500 lb-in, 4875 RPM and 140 °F with $t_c = 0.44$ ms and $f_m = 2275$ Hz: (a) $x_p(t)$, (b) $X_p(f)$, (c) $y_p(t)$ and (d) $Y_p(f)$. --- gear pair with perfect involute profile in t domain (II-A), ○ with perfect involute profile in f domain (II-A) and — with tip relief (II-B).

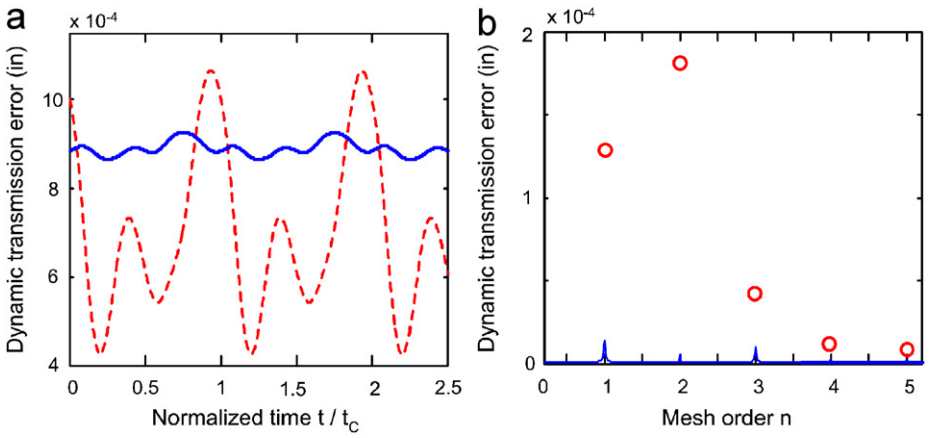

Fig. 15. Dynamic transmission error predicted for Example II at 500 lb-in, 4875 RPM and 140 °F with $t_c = 0.44$ ms and $f_m = 2275$ Hz: (a) $\delta(t)$ and (b) $\Delta(f)$. --- gear pair with perfect involute profile in t domain (II-A), ○ with perfect involute profile in f domain (II-A), and — with tip relief (II-B).

direction and it is minimized at 500 lb-in when the tip relief is applied. An alternative explanation is that the peak-to-peak variation of $\sum N_{pi}$ is minimized with the tip relief as shown in Fig. 13.

In the off-line-of-action direction, more significant oscillations are observed for $y_p(t)$ due to increased $\sum F_{fpi}$ excitations with tip relief. Despite that the vibratory components of $\sum N_{pi}$ are larger than those of $\sum F_{fpi}$, the predicted $y_p(t)$ is actually higher than $x_p(t)$. This shows the necessity of including sliding friction when other excitations such as the static transmission error are minimized. It is worthwhile to notice that a phase difference is present in the simulated $y_p(t)$ before and after the tip relief is applied. Predicted pinion bearing forces are not shown here since they depict the same features shown in the displacement responses of Fig. 14. The dynamic transmission error predictions, as defined by Eq. (17), with and without the tip relief are shown in Fig. 15. From the similarities between Figs. 14(a–b) and 15(a–b) it is implied that the relative line-of-action displacement plays a dominant role in the dynamic transmission error responses. However, this conclusion is somewhat case specific as the dynamic transmission error results depend on the mesh stiffness, bearing stiffness and gear geometry.

7. Experimental validation of Example II models

Experiments corresponding to Example II-B were conducted at the NASA Glenn Research Center (Gear Noise Rig) to validate the multi-degree-of-freedom spur gear pair model and to establish the relative influence of the friction force excitation on the system. Fig. 16 is a photograph of the inside of the gearbox, where a bracket was built to hold two shaft displacement probes one inch away from the center of the gear in the line-of-action and off-line-of-action directions [13]. The probes face a steel collar that was machined to fit around the output shaft with minimal eccentricity. Accelerometers were mounted on the bracket, so the motion of the displacement probes could be subtracted from the measurements, if necessary. A thermocouple was installed inside the gearbox to measure the temperature of the oil flinging off the gears as they enter into mesh. The thermocouple position was chosen to be consistent with Benedict and Kelley's [14] experiment. A common shaft speed of 4875 rpm was used in all tests so that the first five harmonics of the gear mesh frequency (2275, 4550, 6825, 9100, and 11375 Hz) do not excite system resonances. Measurements of shaft displacement in the line-of-action and off-line-of-action directions were collected from the proximity sensors over a range of oil inlet temperatures (104, 122, 140, 158 and 176 °F). At each temperature the torque is varied from 500 to 900 lb-in in steps of 100 lb-in.

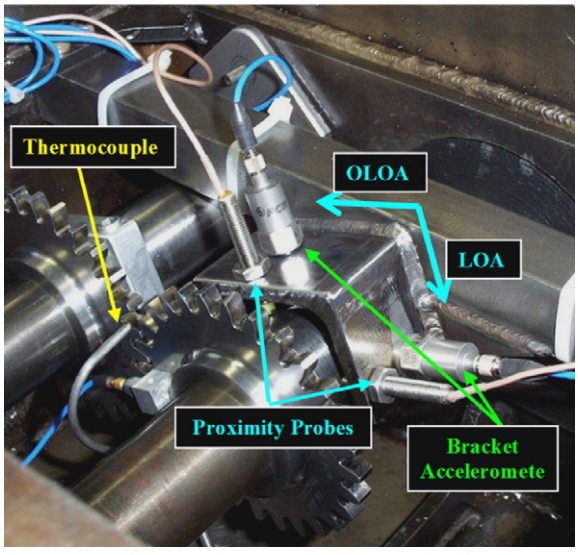

Fig. 16. Sensors inside the NASA gearbox (for Example II-B).

Parametric studies were conducted to examine the dynamic responses under varying operational conditions of temperature and nominal torque. Benedict and Kelly's [14] friction model is used to calculate the empirical μ as given in Table 3 and realistic values of $k(t)$, calculated by using the finite element/contact mechanics code under varying torques, are incorporated into the dynamic model. Since the precise parameters of the experimental system are not known [13], both the simulated and measured data are each normalized with respect to the amplitude of the first mesh harmonic of the off-line-of-action displacement (which is then designated as 100%). This facilitates comparison of trends, i.e., simulations and measurements can be plotted together over the range from 0% to 100%.

The first five mesh harmonics of the line-of-action displacement are shown as a function of mean torque in Fig. 17. (In this and other figures, predictions are shown as continuous lines for the sake of clarity though they are calculated only at discrete points like the measurements). Observe that the overall simulation trend matches the experimental results well. Magnitudes of the first two mesh harmonics are most dominant and they have minimum values around the optimized load due to the linear tip relief. Fig. 17 also shows the predicted first two harmonics for the prefect involute gear (II-A). Compared with the tip relief gear, they increase monotonically with the mean torque and have much higher values than the tip relief gear harmonics around the "optimal" torque.

The first five normalized mesh harmonic amplitudes of the off-line-of-action displacement are shown in Fig. 18, as a function of mean torque. The overall simulation trend again matches the experimental results well. However, unlike the line-of-action responses, the first harmonic of off-line-of-action displacement grows monotonically with an increase in the mean torque. This is because the friction forces increase almost proportionally with normal loads as predicted by the Coulomb law, but the frictional contribution of each meshing tooth pair tends to be in phase with each other for the tip relief gear (II-B). Thus it should amplify the combined friction force excitation in the off-line-of-action direction. Consequently it is not reducing the off-line-of-action direction responses induced by the sliding friction, even though profile modification can be efficiently used to minimize gear vibrations in the line-of-action direction.

The first five mesh harmonics of the normalized dynamic transmission error are shown in Fig. 19 for II-A and II-B cases over a range mean torques. Observe that the dynamic transmission error spectral trends are very similar to the static transmission error spectra of Fig. 10. For example, the harmonic amplitudes of the perfect involute gear grow monotonically with mean torque while the harmonic amplitudes of the tip relief gear have minimum values around the "optimal" torque. Also, the dynamic transmission error spectra show a dominant second harmonic, whose magnitude is comparable to that at the first harmonic. In some cases for

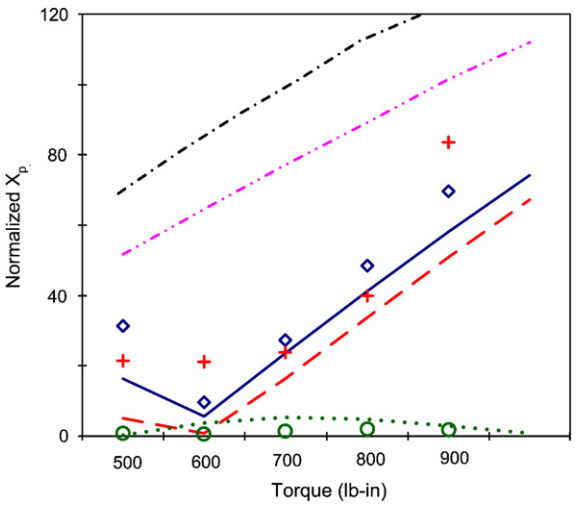

Fig. 17. Mesh harmonic amplitudes of X_p as a function of the mean torque at 140 °F. All values are normalized with respect to the amplitude of Y_p at the first mesh harmonic. — $n = 1$ (prediction of II-B), - - $n = 2$ (prediction of II-B), ····· $n = 3$ (prediction of II-B), –·– $n = 1$ (prediction of II-A), –· ·– $n = 2$ (prediction of II-A), ◇ $n = 1$ (measurement of II-B), + $n = 2$ (measurement of II-B), and ○ $n = 3$ (measurement of II-B).

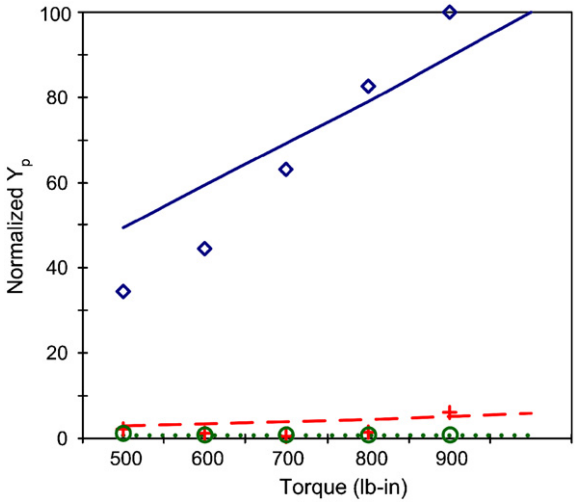

Fig. 18. Mesh harmonic amplitudes of y_p as a function of the mean torque at 140 °F for Example II-B. All values are normalized with respect to the amplitude of y_p at the first mesh harmonic. — $n = 1$ (prediction of II-B), - - $n = 2$ (prediction of II-B), ····· $n = 3$ (prediction of II-B), ◇ $n = 1$ (measurement of II-B), + $n = 2$ (measurement of II-B), and ○ $n = 3$ (measurement of II-B).

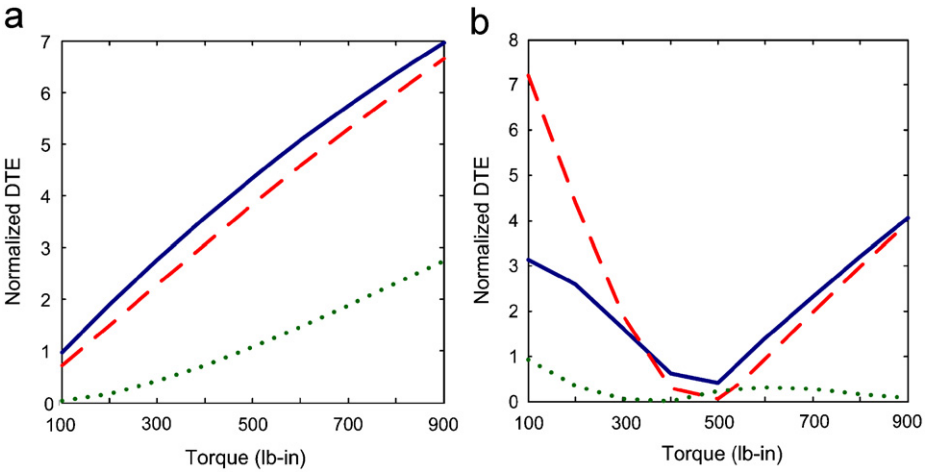

Fig. 19. Predicted dynamic transmission errors (DTE) for Example II over a range of torque at 140 °F: (a) gear pair with perfect involute profile (II-A) and (b) with tip relief (II-B). All values are normalized with respect to the amplitude of δ (II-A) at the first mesh harmonic with 100 lb-in. — $n = 1$ (II-B), - - $n = 2$ (II-B), and ····· $n = 3$ (II-B).

the tip relief gear the second harmonic becomes the most dominant component especially when the mean torque is lower than 350 lb-in.

Finally, the first five mesh harmonics of the normalized line-of-action displacement are shown in Fig. 20 as a function of the operational temperature. The changes in temperature are converted into a variation in friction (μ) by using the data in Table 3. Compared with the off-line-of-action motions, both predictions and measurements in the line-of-action direction give almost identical results at all temperatures. Fig. 21 shows the first five normalized mesh harmonic amplitudes of the off-line-of-action displacement as a function of temperature. The first harmonic varies quite significantly even though the changes in μ are relatively small. Consequently, the off-line-of-action dynamics tends to be much more sensitive than the online action dynamics to a variation in μ. Measured data in Fig. 21 show some variations due to the experimental errors [13].

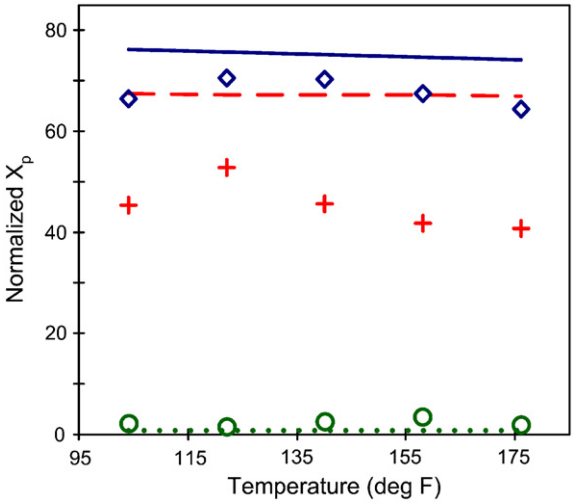

Fig. 20. Mesh harmonic amplitudes of x_p as a function of temperature at 500 lb-in for Example II-B. All values are normalized with respect to the amplitude of y_p at the first mesh harmonic. — $n = 1$ (prediction of II-B), - - $n = 2$ (prediction of II-B), ····· $n = 3$ (prediction of II-B), ◇ $n = 1$ (measurement of II-B), + $n = 2$ (measurement of II-B), and ○ $n = 3$ (measurement of II-B).

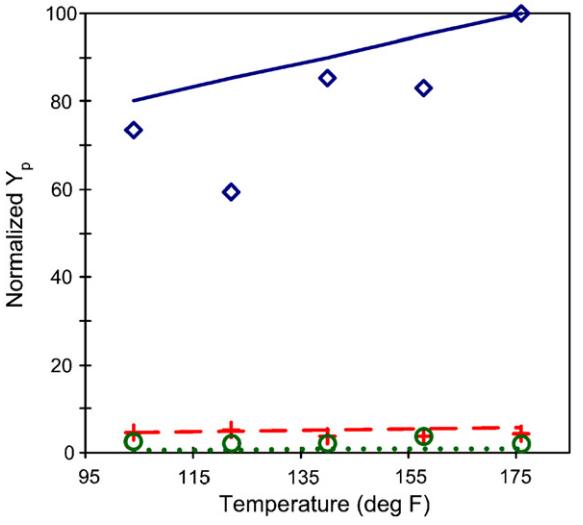

Fig. 21. Mesh harmonic amplitudes of y_p as a function of temperature at 500 lb-in for Example II-B. All values are normalized with respect to the amplitude of y_p at the first mesh harmonic. — $n = 1$ (prediction of II-B), - - $n = 2$ (prediction of II-B), ····· $n = 3$ (prediction of II-B), ◇ $n = 1$ (measurement of II-B), + $n = 2$ (measurement of II-B), and ○ $n = 3$ (measurement of II-B).

8. Conclusion

The chief contribution of this paper is the development of a new multi-degree of freedom, linear time-varying model. This formulation overcomes the deficiency of Vaishya and Singh's work [1–3] by employing realistic tooth stiffness functions and the sliding friction over a range of operational conditions. Refinements include: (1) an accurate representation of tooth contact and spatial variation in tooth mesh stiffness based on a finite element/contact mechanics code in the "static" mode; (2) a Coulomb friction model for sliding resistance with an empirical coefficient of friction that is a function of operation conditions; (3) a better representation of

the coupling between the line-of-action and off-line-of-action directions including torsional and translational degrees of freedom. Numerical solutions of the multi-degree-of-freedom model yield the dynamic transmission error and vibratory motions in the line-of-action and off-line-of-action directions. The new model has been successfully validated first by using the finite element/contact mechanics code while running in the "dynamic" mode and then by analogous experiments. Since the lumped model is more computationally efficient than the finite element/contact mechanics analysis, it could be quickly used to study the effects of varying a large number of parameters.

One of the main effects of sliding friction is the enhancement of the dynamic transmission error magnitude at the second gear mesh harmonic. A key question of whether the sliding friction is indeed the source of the off-line-of-action motions and forces is then answered by our model. The bearing forces in the line-of-action direction are influenced by the normal tooth loads, but the sliding frictional forces primarily excite the off-line-of-action motions. Finally, the effect of the profile modification on the dynamic transmission error has been analytically examined under the influence of frictional effects. For instance, the tip relief introduces an amplification in the off-line-of-action motions and forces due to an out of phase relationship between the normal load and friction forces. This knowledge should be of significant utility to designers. Future modeling work should include an examination of the effects of other profile modifications to determine the conditions for minimal dynamic responses when both static transmission error and friction excitations are simultaneously present. Also, the model could be further refined by incorporating alternative friction formulations.

Acknowledgments

This article is based upon a three-year study that was supported by the US Army Research Laboratory and the US Army Research Office under contract/grant number DAAD19-02-1-0334. This support and the encouragement by Dr. G. L. Anderson (project monitor) are gratefully acknowledged. Dr. S. Vijayakar (Advanced Numerical Solutions, Inc.) is thanked for providing access to the External2D gear analysis software. We acknowledge the experimental work conducted by V. Asnani and the calculation of empirical coefficients of friction performed by A. Holob, both from the Acoustics and Dynamics Laboratory at The Ohio State University; these studies are reported in [15]. Dr. T. Lim from the University of Cincinnati is thanked for providing the Rebm3.0 software for calculation of the bearing stiffness. Finally, we thank the Mechanical Components Branch of the NASA Glenn Research Center for providing us with the experimental facilities.

References

[1] M. Vaishya, R. Singh, Analysis of periodically varying gear mesh systems with Coulomb friction using Floquet theory, *Journal of Sound and Vibration* 243 (3) (2001) 525–545.
[2] M. Vaishya, R. Singh, Sliding friction-induced non-linearity and parametric effects in gear dynamics, *Journal of Sound and Vibration* 248 (4) (2001) 671–694.
[3] M. Vaishya, R. Singh, Strategies for modeling friction in gear dynamics, *ASME Journal of Mechanical Design* 125 (2003) 383–393.
[4] D.R. Houser, M. Vaishya, J.D. Sorenson, Vibro-acoustic effects of friction in gears: an experimental investigation, *SAE* (2001) paper No. 2001-01-1516.
[5] P. Velex, V. Cahouet, Experimental and numerical investigations on the influence of tooth friction in spur and helical gear dynamics, *ASME Journal of Mechanical Design* 122 (4) (2000) 515–522.
[6] P. Velex, P. Sainsot, An analytical study of tooth friction excitations in spur and helical hears, *Mechanism and Machine Theory* 37 (2002) 641–658.
[7] O. Lundvall, N. Strömberg, A. Klarbring, A flexible multi-body approach for frictional contact in spur gears, *Journal of Sound and Vibration* 278 (3) (2004) 479–499.
[8] External2D (CALYX software), *A contact mechanics/finite element (CM/FE) tool for spur gear design*, ANSOL Inc., Hilliard, OH.
[9] H. Vinayak, R. Singh, C. Padmanabhan, Linear dynamic analysis of multi-mesh transmissions containing external, rigid gears, *Journal of Sound and Vibration* 185 (1) (1995) 1–32.
[10] T.C. Lim, R. Singh, Vibration transmission through rolling element bearings. Part I: bearing stiffness formulation, *Journal of Sound and Vibration* 139 (2) (1990) 179–199.
[11] T.C. Lim, R. Singh, Vibration transmission through rolling element bearings. Part II: system studies, *Journal of Sound and Vibration* 139 (2) (1991) 201–225.

[12] A. Kahraman, R. Singh, Error associated with a reduced order linear model of spur gear pair, *Journal of Sound and Vibration* 149 (3) (1991) 495–498.
[13] R. Singh, Dynamic analysis of sliding friction in rotorcraft geared systems, technical report submitted to the Army Research Office, grant number DAAD19-02-1-0334, 2005.
[14] G.H. Benedict, B.W. Kelley, Instantaneous coefficients of gear tooth friction, *Transactions of the American Society of Lubrication Engineers* 4 (1961) 59–70.
[15] B. Rebbechi, F.B. Oswald, D.P. Townsend, measurement of gear tooth dynamic friction, *ASME Power Transmission and Gearing Conference proceedings* DE-Vol. 88, 1996, pp. 355–363.